Journal of Mining and Environment (JME), Vol. 15, No. 2, 2024, 649-665

Shahrood University of Technology

Journal of Mining and Environment (JME)

Journal homepage: www.jme.shahroodut.ac.ir

Iranian Society of Mining Engineering (IRSME)

Classification of ASTER Data by Neural Network to Mapping Alterations Related to Copper and Iron Mineralization in Birjand

Jabar Habashi[1], Majid Mohammady Oskouei[1*], and Hadi Jamshid Moghadam[2]

1. Faculty of Mining Engineering, Sahand University of Technology, Tabriz, Iran
2. head of the R&D department of Foladgostar Kowsar Investment Group, Iran

Article Info

Received 20 September 2023
Received in Revised form 6 November 2023
Accepted 12 November 2023
Published online 12 November 2023

DOI: 10.22044/jme.2023.13652.2525

Keywords

Remote sensing
ASTER
Neural network
Porphyry copper
Advanced argillic

Abstract

The studied area located in eastern Iran shows a high potential for various mineralizations, especially copper due to its tectonic activity. Remote sensing data can effectively distinguish these areas because of the sparse vegetation. Therefore, in this study, the ASTER (Advanced Spaceborne Thermal Emission and Reflection Radiometer) multi-spectral data was used to recognize argillic, sericite, propylitic, and iron oxide alterations associated with copper mineralization. For this purpose, two categories (porphyry copper-iron and advanced argillic-iron) related alterations were considered to perform the classification of a 2617 square kilometer area using a neural network classification algorithm. To evaluate the accuracy of the classifier, the confusion matrix was computed, which provides overall accuracy and the kappa coefficient factors for assessing classification accuracy. As a result, 64.17% and 83.5% of overall accuracy, and 0.602 and 0.807 of the kappa coefficient were achieved for the advanced argillic alterations and porphyry copper categories, respectively. Ultimately, the validation of the classifications was carried out using the normalized score (NS) equation, employing quantitative criteria. Notably, the advanced argillic class emerged with the top normalized score of 2.25 out of 4, signifying a 56% alignment with the geological characteristics of the region. Consequently, this outcome has led to the identification of favorable areas in the central and northeastern parts of the studied area.

1. Introduction

Mineral exploration tasks are generally time-consuming and costly. Remote sensing is a modern exploration method that helps faster and cost-effective minerals. Satellite data is therefore predominantly used in the initial exploration stages to identify prospective targets[1].

The remote sensing process utilizes the interactions between radiation waves and the target surface. When electromagnetic waves from a source are scattered to the earth's surface, they interact and collide with the atmosphere along their path of travel. This interaction can also occur when energy is transmitted from the earth's surface toward the sensor. The mutual effect of these interactions depends on the surface and the radiation characteristics. After the energy is scattered and reflected by the earth, we need a sensor to collect and record the electromagnetic waves [4–2].

One of the applications of remote sensing in the field of mining is the identification of various geological alterations, especially hydrothermal alterations associated with porphyry copper. These alterations occur through hydrothermal processes that alter the mineralogy and chemical composition of the surrounding rocks [5–7].

Mineral alteration leads to the formation of unique mineral assemblages with distinctive spectral absorption features in the visible and near-infrared (VNIR) to short-wave infrared (SWIR) regions (0.4-2.5 micrometers) and the thermal

✉ *Corresponding author: mohammady@sut.ac.ir (M. Mohammady Oskouei)*

infrared (TIR) region (8.0-14.0 micrometers) [8–10].

porphyry copper deposits are commonly associated with hydrothermal alteration zones such as propylitic, argillic, phyllic, and potassic zones [11]. These hydrothermal alteration zones exhibit distinct spectral absorption features in the visible and near-infrared (VNIR) and short-wave infrared (SWIR) regions. By using spectral analysis of these regions, it is possible to identify and characterize the specific minerals associated with these alteration zones. The mineral alteration processes around porphyry copper deposits generate oxidized zones with iron oxide/hydroxide minerals (typically yellow to red-colored altered rocks), commonly referred to as gossans [12,13].

Iron oxide/hydroxide minerals such as limonite, goethite, and hematite exhibit lower reflectance in the visible region and higher reflectance in the near-infrared region. In the crystal structure of these minerals, electron processes create absorption features in the visible and near-infrared wavelengths (0.4 to 1.1 micrometers) due to the presence of transition elements such as Fe^{2+}, Fe^{3+}, and, in some cases, substitution by Mn, Cr, and Ni[7,14].

Hydroxide-bearing minerals including clays and sulfate groups, as well as carbonate minerals, exhibit distinctive spectral absorption characteristics in the shortwave infrared region of the electromagnetic spectrum due to fundamental vibrational absorption processes. These absorption features arise from vibrational processes of aluminum-oxygen-hydrogen (Al-O-H), magnesium-oxygen-hydrogen (Mg-O-H), silicon-oxygen-hydrogen (Si-O-H) linkages, and CO_3 groups in the shortwave infrared region [7,14–16].

Therefore, shortwave infrared (SWIR) data can be used to identify thermally altered mineral assemblages including (a) mineralized zones formed by the passage of low-pH fluids (such as alunite and pyrophyllite). (b) mineral materials containing Al-Si-(OH) and Mg-Si-(OH) groups including kaolinite, mica, and chlorite. (c) mineral materials containing Ca-Al-Si-(OH) such as the epidote group, as well as carbonate groups (calcite and dolomite) [17].

Minerals associated with hydrothermal alterations, characterized by diagnostic spectral absorption features in the visible to near-infrared and shortwave infrared regions, can be identified and classified using multi-spectral and hyperspectral data. This information can be used in the initial exploration process for porphyry copper and epithermal gold mineralization [18–28].

Distinguishing between three hydrothermal alterations, particularly identifying phyllic alteration, is crucial in the exploration of porphyry copper deposits as the phyllic zone indicates high economic potential for copper mineralization in the mineralized crust [29].

One of the most commonly used sensors in remote sensing exploration is the ASTER sensor. The ASTER sensor has 14 spectral bands, with 4 bands in the near-infrared range (with a spatial resolution of 15 meters), 6 bands in the shortwave infrared range (with a spatial resolution of 30 meters), and 5 bands in the thermal infrared range (with a spatial resolution of 90 meters). The ASTER sensor consists of six infrared bands, which are highly valuable for geological applications, particularly mineralogical studies. Additionally, the five thermal bands are utilized to accurately estimate surface temperature and measure various phenomena [30].

2. ASTER Data

Karimpour *et al*. described the classification of erosion levels in three porphyry copper deposits, namely Maherabad, Shadan, and Chah Shaljami, which are situated within the volcanic-plutonic belt of the Lut block. The distributions of end-members were mapped using Spectral Angle Mapper (SAM) and Mixture Tuned Matched Filtering (MTMF) techniques on the Visible and Near Infrared (VNIR) and Shortwave Infrared (SWIR) bands of ASTER data. The findings were then compared to field studies. The ASTER sensor data proved successful in distinguishing and providing explanations for the different erosion levels observed in porphyry copper deposits [31].

Mohebi *et al*. provided an account of the identifying structural factors influencing the modification and mineralization processes in the vicinity of Hanza Mountain [32]. Sojdehee *et al*. outlined the process of distinguishing hydrothermal alteration zones by utilizing SWIR data at the Daralu copper deposit [33]. Farahbanksh merged ASTER and QuickBird data to effectively portray the nature and attributes of the Naysian porphyry copper deposit [34]. Yousefi *et al*. employed SWIR and TIR data to distinguish alteration zones, enabling the cartographic representation of sericite, phyllic, and quartz-rich alteration zones within the Kerman magmatic arc [35,36].

Another category of reports related to the copper deposits in Iran focused on utilizing ASTER data as an exploratory instrument to

recognize potential prospects. Typically, this involved extracting valuable information through the analysis of proved deposits and expanding it to areas that have received limited or no exploration. The utilization of ASTER SWIR data was highlighted by Pour and Hashim within the Urumieh-Dokhtar volcanic belt. In this case, by employing a model based on porphyry copper formations, which proposed concentric alteration zones with distinct mineral compositions, potential prospects were successfully identified [37]. Honarpazhouh integrated stream sediment geochemistry with ASTER data in the Khatun Abad region. This combined approach proved to be a superior exploration strategy compared to solely relying on remote sensing data [38]. Pazand et al. employed ASTER data as part of their preliminary exploration efforts to identify porphyry copper mineralization in the Ahar region [39]. Within the Daraloo-Sarmeshk region, Alimohammadi *et al.* utilized ASTER data to conduct exploration activities aimed at identifying undiscovered copper deposits. Specifically, ASTER SWIR data was employed to emphasize alteration zones, facilitating the detection of potential mineralization [40]. Yazdi *et al*. documented similar endeavors in their reported projects [41].

Mars and Rowan made a notable contribution in 2006 by presenting one of the most effective utilization of ASTER data for regional mineral exploration within a copper belt. They constructed a mosaic of 62 ASTER scenes containing a vast 900 km-wide belt located in the Zagros magmatic arc of Iran. Their approach involved devising a series of logical operators, incorporating band ratios and thresholds of ASTER data, to accentuate the image of spectral absorption characteristics linked to phyllic and argillic alteration [42].

Research conducted in various parts of the globe contains investigations such as Carrino *et al*.'s studies in the Chapi Chiara region situated in southern Peru. In their study, ASTER data was utilized to cartographically depict the geological characteristics and alteration mineralogy of the area, to identify potential copper targets [43].

Rajendran and Nasir investigated determining alteration zones associated with volcanogenic massive sulfide deposits by examining the spectral response of ASTER bands. This approach according to analyzing multiple established deposits was effective in mapping and characterizing alteration zones [44]. Zhang and Zhou conducted further research in China, specifically focusing on the Baogutu porphyry copper deposit. They employed ASTER data to detect and delineate the corresponding alteration zones. This valuable information can subsequently be utilized to explore other adjacent regions exhibiting similar geological characteristics [45].

Within the Bangonghu-Nujiang metallogenic belt in Tibet, Dai *et al*. employed ASTER data to identify alterations, and show distinct spectral attributes associated with desired mineralogical compositions [46].

In this research work, based on comprehensive studies on the application of the ASTER sensor in identifying mineralization-prone areas for copper, the use of band ratios related to hydrothermal alterations has been emphasized. To identify areas prone to porphyry copper and advanced argillic alterations in the sar-e-châh-e-shur region, a neural network algorithm was employed for classification. The accuracy of the classification algorithm results was calculated using the confusion matrix. In the category related to advanced argillic, an overall accuracy of 64.17% and a kappa coefficient of 0.602 were achieved. Additionally, in the category related to porphyry copper, an overall accuracy of 83.5% and a kappa coefficient of 0.807 were obtained. Finally, the normalized score (NS) equation was utilized to quantify the qualitative components of conformity and estimation level for a better understanding of the validation level. In this study, the classification results of the training data related to advanced argillic obtained a normalized score of 2.25 out of 4, which corresponds to 56%. These results outperformed the classification results of the training data related to porphyry copper and exhibited better conformity with the existing reality. This approach led to the identification of prospective areas in the central and northeastern parts of the studied area.

3. Studied Area

The area is situated in Birjand, Iran, within the geographical coordinates of 32° to 32°30' N and 58°30' to 59°E.

The area in question is commonly known as the Sistan structural zone. In the past, the eastern part of Iran, specifically the Lut Block, has witnessed substantial tectonic activity, accompanied by extensive volcanic activity. Consequently, this region holds significant promise for a variety of mineral deposits, with a particular emphasis on copper mineralization [47].

The simplified geological map in Figure 1 depicts the region. The key geological units in the area are composed of Eocene-Oligocene volcanic

rocks, with some intrusive bodies of semi-deep acidic to intermediate alkali calc-alkaline porphyritic textures. The volcanic rocks mainly consist of dacite, diorite, granite, dolerite dikes, diabase, gabbro, and olivine basalt. The sedimentary rocks include shale and sandstone, oolitic limestone, limestone, conglomerate, and metamorphic facies such as gneiss, metagabbro, metadiabase, amphibolite schist, chlorite schist, and phyllite. The emplacement of intrusive bodies has also caused varying degrees of metamorphism in the adjacent rocks, ranging from low to high [48].

Most of the lithologies of the region have Syncline and anticlinal folds. The highest concentration of faults and fractures occur in the northern and northeastern parts of the region[48]. Most of the rocks present in the northeastern part of the map have been significantly affected by moderate to intense alteration. Among the mineral indicators in the study area, copper mineralizations such as Chah-e-Tuni, Homich, and Fasson can be mentioned [49].

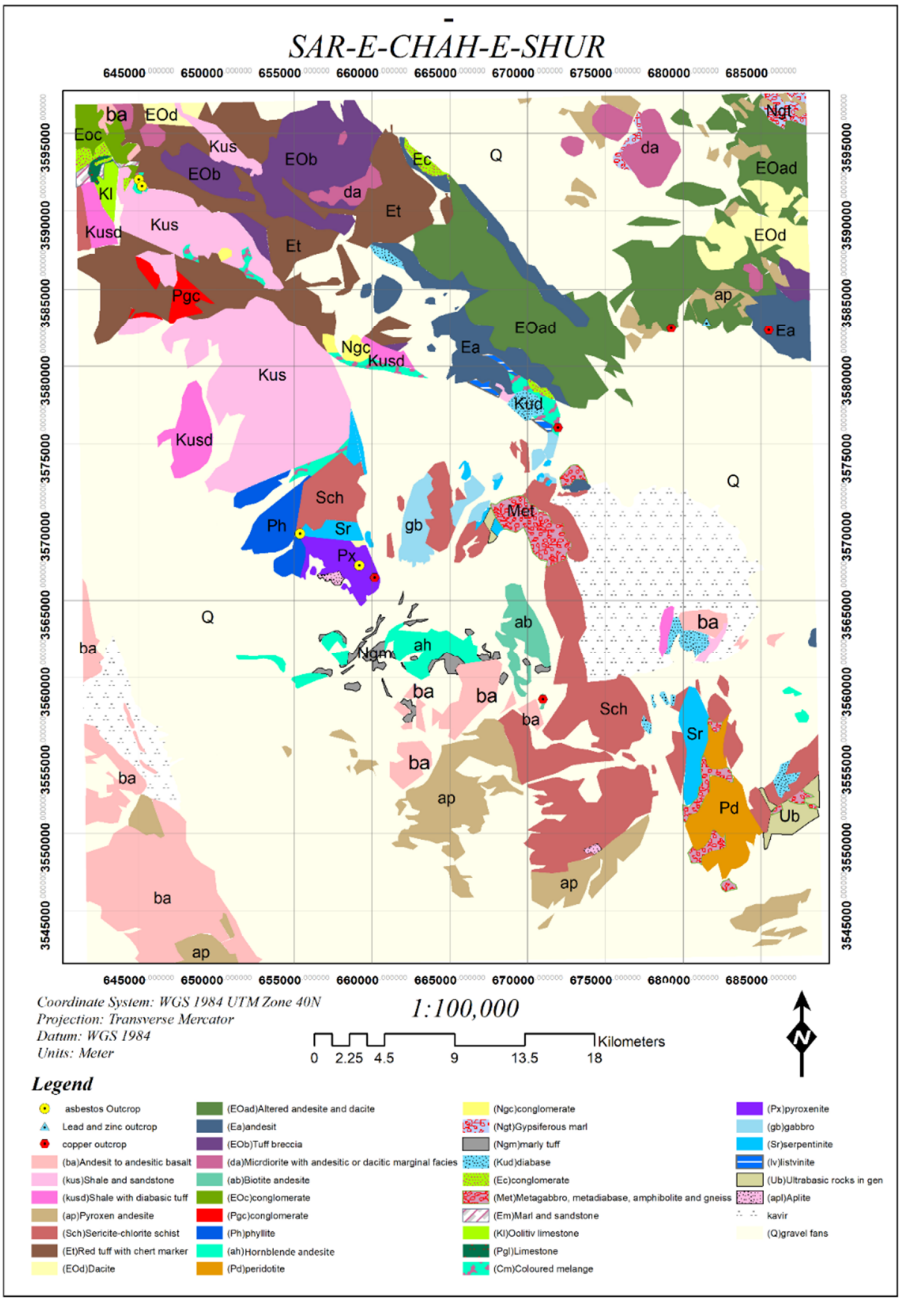

Figure 1. The 1:100,000 simplified geological map of the sar-châh-e-Shur well area.

4. Materials and Methods

To utilize remote sensing images, it is necessary to perform geometric and radiometric pre-processing on the raw images to prepare the data and obtain more comprehensive information. Remote sensing images generally suffer from errors in geometry and radiometric values. The first case of these errors is referred to as a geometric error, while the second error is radiometric. Radiometric errors can be caused by data acquisition devices, solar radiation wavelength, and atmospheric effects [30].

This study utilizes Level-1T (L1T) processed ASTER images, which have undergone geometric and radiometric corrections. Additionally, for atmospheric correction, the logarithmic residual (log-residual) correction technique is employed, which generates a pseudo-reflectance image. The log-residual correction tool is designed to remove the effects of solar radiation, atmospheric transmissivity, instrument efficiency, topographic effects, and albedo effects from the data. This transformation creates a more realistic image of reflectance.

The log-residual correction is applied to the dataset by dividing the input spectrum by the spectral geometric mean, and then dividing it by the spatial geometric mean. The use of the geometric mean is chosen because it accounts for the transmittance and other multiplicative effects. The calculation of the geometric mean is performed using the logarithm of the data values. The spectral geometric mean represents the average for all bands in each pixel and removes topographic effects. The spatial geometric mean represents the average of all pixels for each band and takes into account solar radiation, atmospheric transmissivity, and instrument efficiency. The log-residual calibration utilizes intrinsic image statistics to generate a calibrated outcome, and does not consider external calibrated data [50].

In summary, the logarithmic residual calibration tool is a useful pre-processing technique for radiance data, enabling the extraction and analysis of relevant spectral absorption features related to mineral materials. By removing various effects from the data, it creates a more realistic reflectance image, facilitating further analysis [50]. Figure 2 illustrates the spectral profile of a pixel in the ASTER images pre and post-log-residual atmospheric correction. It shows the alterations in the pixel's spectral characteristics resulting from the correction.

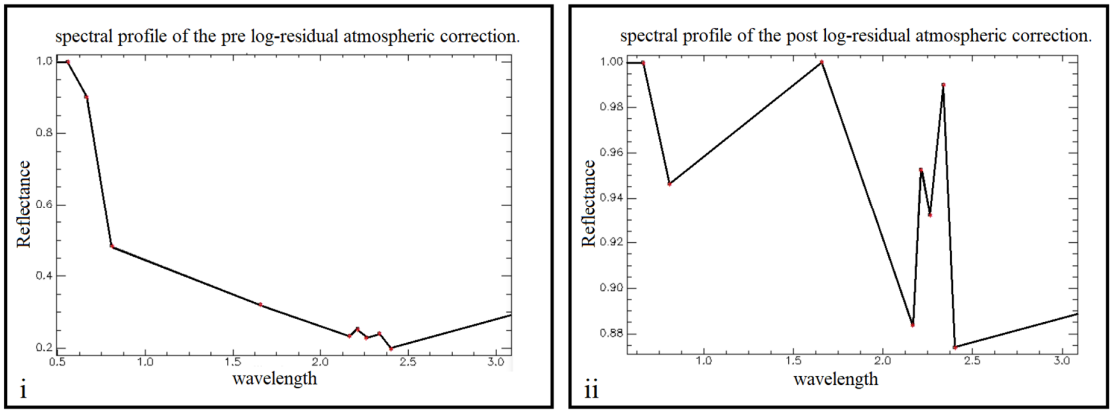

Figure 2. The spectral profile of a pixel in the ASTER images pre (i) and post (ii) log-residual atmospheric correction.

5. Data Processing

In the field of remote sensing, a variety of methods are employed for the analysis of images acquired from the Earth's surface. The division and ratio of pixel values across different bands is a valid technique for reducing the impact of certain phenomena in the image and identifying specific anomalies in different land cover types [51,52].

This method involves dividing, adding or multiplying two or more bands together. The band with a higher reflectance of the target under investigation is placed in the numerator, while the band with a higher absorption effect for the same target is placed in the denominator. By employing this technique, it is possible to decrease the effects of topography and shadows in the image, reveal the contrast between brightness values, and use it for delineating geological boundaries and identifying rocks [53].

Given that mineralogy and lithology are important aspects of geology and related studies,

the utilization of ASTER band data such as SWIR, VNIR, and TIR is highly beneficial. In particular, the use of VNIR bands is valuable for determining chlorophyll absorption in plants and certain metals, especially iron and rare earth elements. Additionally, the utilization of SWIR bands can provide crucial information regarding the molecular absorption characteristics of mineral materials, which are essential for studying the structure and properties of rocks and minerals. Generally, the significant use of ASTER band data in satellite imagery can contribute to the identification of mineralogical and lithological features [53].

Iron compounds exist in nature with various structures. To identify iron compounds using satellite imagery, different band ratios in the SWIR and VNIR bands are utilized. Iron compounds are commonly found in the form of Fe^{2+} and Fe^{3+} in oxides such as magnetite (Fe_3O_4) and hematite (Fe_2O_3) or as hydroxides like goethite (FeO.OH). Additionally, there are numerous iron oxidation states represented by compounds such as iron sulfate ($FeSO_4$), iron chloride ($FeCl_3$), magnetite, and potassium ferrate (K_2FeO_4), indicating the presence of iron oxide and hydroxide-rich areas in the region. These areas result from weathering and oxidation of iron sulfide minerals such as pyrite and chalcopyrite. Therefore, based on the mentioned explanations, band ratios related to iron alterations were created. The band ratio of 4/3 is used to enhance the detection of iron oxide alterations [54]. The band ratio of 4/2 is used to enhance the detection of gossan. Gossan is a part of oxidized and hydroxylated iron and manganese deposits that are often observed in yellowish to brownish colors. Gossans have been widely used as key indicators for the exploration and mining of gold and silver deposits [55].

The ratio of 4/5 is particularly useful in enhancing the detection of silicate minerals such as biotite, chlorite, and amphibole within a given area. This ratio can provide indications of the presence of these minerals. Moreover, it has been employed as an index for identifying gold and copper alterations [54]. Also the band ratio 4/5 is utilized to enhance the detection of muscovite, illite, and laterite minerals [56] in the area. By applying this ratio, these specific mineral types can be identified and analyzed.

Furthermore, the band ratio 4/8 is commonly utilized for identifying mineral assemblages consisting of epidote, chlorite, and amphibole [54]. This ratio proves to be an effective indicator of the presence of these minerals in a given region. Additionally, it can serve as a valuable tool for identifying propylitic and skarn alterations within the area [57]. The use of the 4/8 band ratio enables the researchers to identify and study these specific mineral assemblages and alteration types accurately.

In addition, the band ratio of 4/6 has been used to identify kaolinite minerals in the region, indicating the presence of an argillic zone[57]. Other band ratios used in this study include the following cases.

The band ratio 5/6 was used to identify the mineral phengite, while the ratio 7/6 was utilized to enhance the visibility of muscovite. Also the ratio 7/5 was employed to highlight the mineral kaolinite in the region, resulting in the creation of bright white and gray colors in the generated images, indicating mineralization associated with the band ratio [54].

Finally, to enhance area differentiation and minimize errors, the Normalized Difference Vegetation Index (NDVI) is commonly employed in remote sensing. This simple graphical index is extensively utilized to evaluate vegetation cover presence or absence. It is calculated by taking the band ratio of (3-2)/(3+2) from ASTER imagery, generating the NDVI index [58].

Using these proportions allows us to detect and examine particular types of minerals, leading to the manifestation of a stark white hue within the black-and-white shades in the produced images. Furthermore, in Figure 3, the purest pixels (approximately 0.3% of all pixels) belonging to these classes are emphasized by red-colored regions of interest (ROIs). These pixels serve as the basis for subsequent processes, and we will furnish a comprehensive description of each classification.

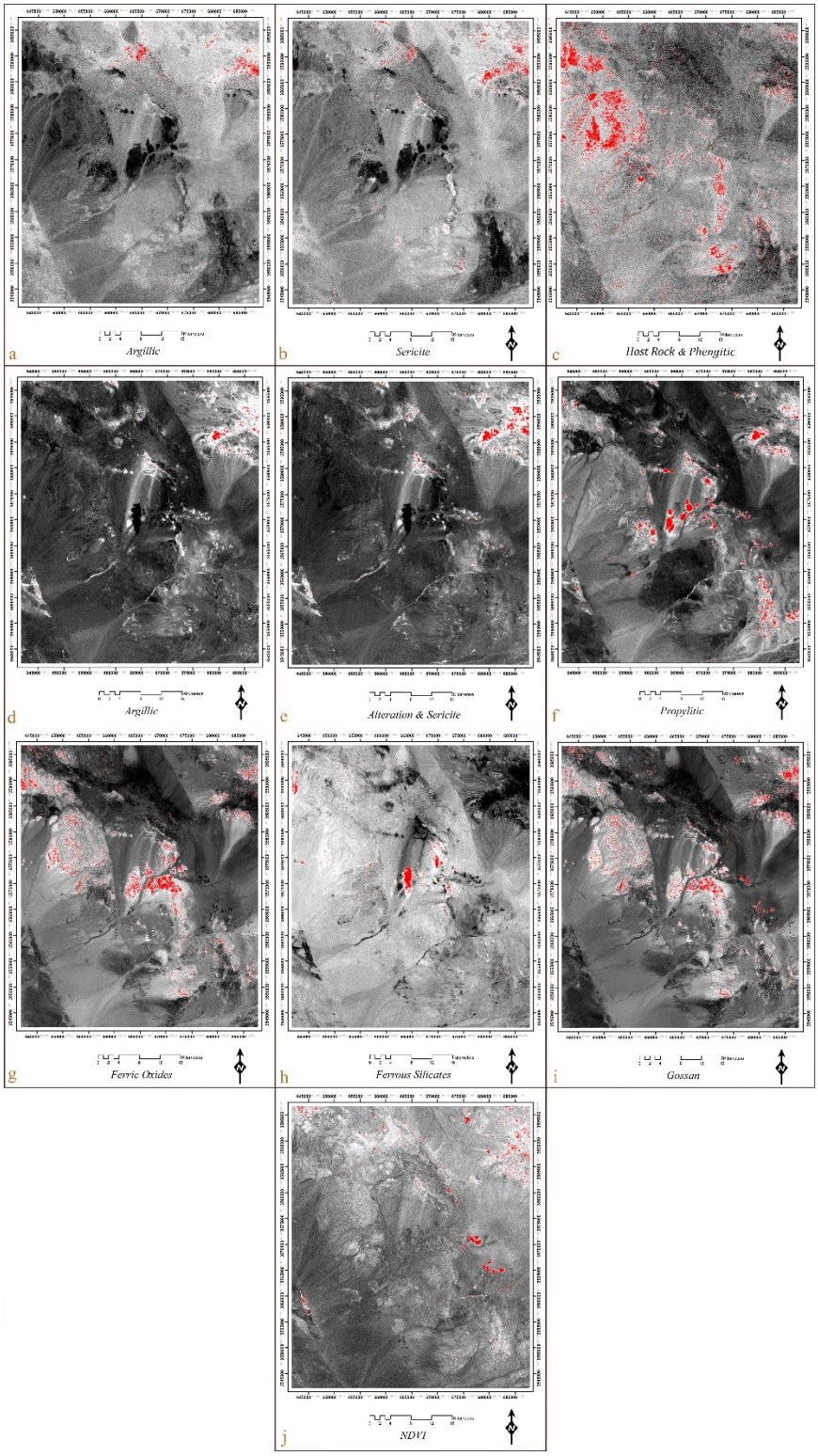

Figure 3. (a) Band ratios: (7/5) for identifying Argillic (Kaolinite) alteration [59], (b) band ratio (7/6) for identifying Sericite (Muscovite) alteration [57], (c) band ratio (5/6) for identifying host rock & Propylitic (Host rock, phengitic) alteration [56], (d) band ratio (4/6) for identifying Argillic (Kaolinite) alteration [57], (e) band ratio (4/5) for identifying Sericite & Alteration (Muscovite, laterite) alteration [56], (f) band ratio (4/8) for identifying Propylitic (Colerit) alteration [57], (g) band ratio (4/3) for identifying ferric oxides alteration [59], (h) band ratio (5/4) for identifying ferrous silicates alteration [59], (i) band ratio (4/2) for identifying Gossan alteration [56], (j) band ratio (3-2)/(3+2) for identifying NDVI [58].

6. Category of Classes

To ensure a meticulous and accurate analysis of the region, it is crucial to establish precise and comprehensive training categories. With this objective in mind, we have defined two distinct sets of training data: one focusing on porphyry-copper and iron alterations, and the other centered on advanced argillic and iron alterations. This decision stems from the observation that incorporating multiple classes with similar applications in classification concurrently can lead to reduced accuracy in abundance maps and potentially create confusion during their interpretation.

For instance, using 4/5, 4/6, and 4/8 band ratios to identify sericite, propylitic, and argillic alterations is useful for detecting areas favorable for porphyry copper [57]. On the other hand, classes were also created using 5/6, 7/6, and 7/5 band ratios to identify phengitic, sericite, and argillic alterations, which are used for detecting advanced argillic zones [59].

Therefore, based on the provided information and introduced band ratios, two categories of classes have been designed as follows:

1. Catagory A-1: This category is used to highlight porphyry copper alterations, gossan areas, Iron Silicate, iron oxides, and normalized difference vegetation index (Table 1).
2. Category A-2: This category is used to highlight advanced argillic alterations, gossan areas, iron silicate, iron oxides, and normalized difference vegetation index (Table 1).

Table 1. The created categories and the corresponding band ratios

Aster category A-1		Aster category A-2	
Alteration	**Band ratio**	**Alteration**	**Band ratio**
Alteration [56] & Sericite [57]	4/5	Alteration [56]	**4/5**
Argillic [57]	4/6	Sericite [57]	**7/6**
Propylitic [57]	4/8	Ferric oxides [59]	**4/3**
Ferric oxides [59]	4/3	ferrous silicates [59]	**5/4**
Ferrous silicates [59]	5/4	NDVI [58]	**3-2/3+2**
NDVI [58]	3-2/3+2	Gossan [56]	**4/2**
Gossan [56]	4/2	Host rock [56] & [59] Propylitic	**5/6**
Host rock [56]	5/6	Argillic [59]	**7/5**

7. Separability of Classes

Separability refers to spectral discrimination, and is employed in the domain of remote sensing image processing. This concept denotes the extent to which two distinct regions in a digital image are distinguishable from each other based on their spectral characteristics.

Spectral separability is computed using two metrics, namely the Jeffries-Matusita separability and the Transformed Divergence, between selected class pairs within an input file. These values range from 0 to 2.0 and signify the statistical distinctiveness between the chosen class pairs. Values exceeding 1.5 indicate a significant separability among the class pairs, indicating their clear separation. For class pairs with lower separability values, enhancing their separability can be achieved through class refinement or the selection of new classes. In cases where the separability values are extremely low (below 1), combining them into a single class can be considered [60].

With examining the initial separability of the input classes, a high overlap between the sericite and argillic classes was observed within category A-1. Consequently, these two classes were merged into a single class called "Alteration, Sericite & Argillic". The results of the final separability of the training classes can be seen in Tables 2 and 3. In Table 2, the separability value of the classes A-1 has been measured. All input classes exhibit spectral separability from each other, and the minimum separability value among class pairs, specifically between gossan and iron oxides, exceeds 1.56, which is considered acceptable. Additionally, in Table 3, the separability value of the classes A-2 has been measured all the input classes show spectral separability of each other, and the minimum value of separability between pairs of classes belongs to argillic and sericite, which is more than 1.53, which is considered acceptable.

Therefore, considering the acceptable separability between the class pairs within the two presented categories in Tables 2 and 3, it is possible to utilize these two categories in the final classification.

Table 2. Value of the separability measure of class A-1.

A-1 separability	Host rock	Gossan	NDVI	Ferrous silicates	Ferric oxides	Propylitic
Alteration & Sericite & Argillic	2	1.89	1.90	2	1.99	1.96
Propylitic	2	1.91	1.95	2	1.98	
Ferric oxides	1.91	**1.56**	2	1.86		
Ferrous silicates	1.96	1.97	2			
NDVI	2	1.83				
Gossan	1.96					

Table 3. Value of the separability measure of class A-2.

A-2 separability	Gossan	NDVI	Ferrous silicates	Ferric oxides	Argillic	Sericite	Propylitic& host rock
Alteration	1.90	1.91	2	2	1.68	1.76	1.99
Host rock & Propylitic	1.96	2	1.96	1.91	2	1.92	
Sericite	1.96	1.97	2	1.98	**1.53**		
Argillic	1.98	1.97	2	2			
Ferric oxides	1.56	2	1.86				
Ferrous silicates	1.97	2					
NDVI	1.83						

8. Results

To better understand the studied area in the field of remote sensing, a method called "classification" is utilized. In this method, classes are defined, each representing pure pixels from the image and corresponding to a specific mineral or geological feature. In this case, regions that do not contain pure pixels are classified as part of each respective class.

Neural networks are a powerful and widely used method in the field of machine learning and data analysis, inspired by the structure and functioning of the human neural system. This method enables us to automatically perform classification, detection, and prediction of data patterns and complex relationships in the data without the need for strong algorithms[61].

In recent decades, with the advancement of technology and the development of artificial intelligence methods, neural networks have gained high popularity as a powerful tool for data analysis and classification. Neural networks, with their ability to recognize patterns and complex relationships in data, can assist us in gaining a deeper understanding of the data and the existing relationships within it[62].

A neural network consists of a set of processing units called neurons, which are interconnected and arranged in different layers. Each neuron receives information and processes it using specific activation functions such as the sigmoid (logistic) function or hyperbolic tangent function to produce output. The different layers of a neural network can include an input layer, hidden layers, and an output layer. Connections between neurons are established with specific weights, and by determining and adjusting these weights, the neural network is capable of learning and adapting to input data [61,63–66].

To train a neural network, it is necessary to first provide the network with training data, and then iteratively adjust the weights using optimization algorithms. In this process, the distance between the output generated by the network and the expected output is minimized to increase the accuracy and correctness of classification. This process is repeated until the network achieves the desired results and the weights are optimally adjusted [64].

Neural networks have applications in various scientific and industrial fields. In the domain of spectral classification, neural networks can be used for analyzing different spectra and detecting specific features in the data [61,63,65].

Neural networks have garnered significant attention due to numerous advantages. Some of these advantages include their ability to recognize patterns in data, their capability to handle complex datasets, their flexibility in adapting to different problem domains, and their potential for network expansion and improvement through techniques like deep learning[63].

To configure the algorithm for classification, certain parameters need to be set. Among these parameters are the number of hidden layers and the number of training iterations. These choices are influenced by the available specific problem and the complexity of the data. It is important to note

that there is no optimal solution, and determining the best values often requires experimentation and fine-tuning [67].

For linear classification, where the input regions can be separated by a single hyperplane, it is sufficient to assign a value of 0 to the number of hidden layers. In the case of non-linear classifications, where the input regions are not linearly separable and need multiple hyperplanes to distinguish between classes, it is typically recommended to assign a value of 1 or more to the number of hidden layers. The precise number of hidden layers needed depends on the complexity of the problem [67].

The number of training iterations signifies the frequency at which the training data is processed through the neural network during the training process. There is no fixed value for this parameter, as it relies on factors such as the size of the training data, the complexity of the problem, and the convergence rate of the training algorithm. Increasing the number of training iterations entails a trade-off, balancing the potential enhancement of accuracy with the increased training time, and computational resources [61]. According to the discussed concepts in this research work, to enhance accuracy and precision in classification, 1000 iterations, and one hidden layer were utilized for non-linear classification. In Figure 3, the neural network classification using classes A-1 (i) and A-2 (ii) is illustrated.

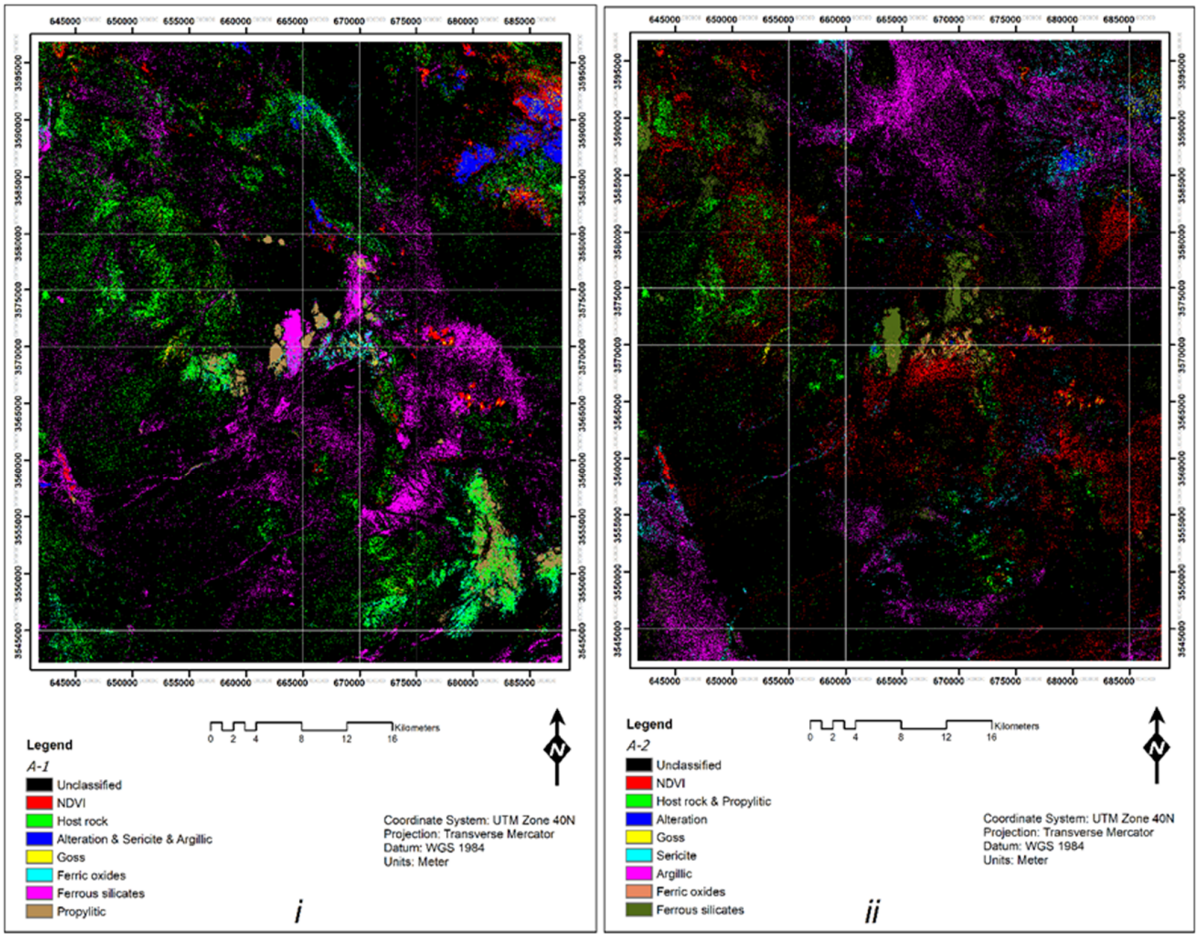

Figure 4. The neural network classification using classes A-1 (i) and A-2 (ii)

9. Discussion

In remote sensing, classification algorithms are not perfect and can have errors and limitations. By evaluating their accuracy and correctness, we can assess their performance and ensure the accuracy of the results.

The results obtained from image analysis in remote sensing can have significant implications for decision-making processes such as identifying

geochemical alterations and monitoring the environment. Therefore, the accuracy and precision of the results are crucial because incorrect decisions based on inaccurate information can have serious consequences.

In summary, classification evaluation is essential in remote sensing tasks to ensure the reliability of the results, evaluate the performance of algorithms, and compare different methods. The use of a confusion matrix in this investigation is a common approach to assess the accuracy of classifications. The confusion matrix compares the classification results with ground truth information and provides a better understanding of the algorithm's performance [68].

This matrix can be computed using either ground truth images or ROI (Region of Interest) of input classes. In both cases, metrics such as overall accuracy, producer's accuracy, user's accuracy, and kappa coefficient are reported [69].

Overall accuracy is a metric that determines the ratio of correctly classified pixels to the total number of pixels. To calculate it, we sum up the number of correctly classified pixels and divide it by the total number of pixels. The ground truth image or actual ROI specifies the true class of the pixels. The correctly classified pixels are located on the diagonal of the confusion matrix, indicating the number of pixels classified correctly. The total number of pixels is equivalent to the sum of all pixels across all true classes [69].

The Kappa coefficient is a metric used in evaluating the accuracy of classifications and agreement in classification problems. This measure quantifies the level of agreement between predicted results and ground truth outcomes, indicating the accuracy and generalizability of the classifications. The kappa coefficient is calculated from the confusion matrix, and in cases where the classification is completely random from one category to another, its value will be zero. In this case, a value of 1 indicates perfect agreement between the predicted and actual classifications [69].

Table 4 presents the results of the confusion matrix, illustrating classifications related to two categories. These results demonstrate that both classifications have high accuracy.

Considering the high accuracy of these two classifications, it can be concluded that the class of categories has been effective in creating valid and efficient classifications. Furthermore, the classification model has successfully assigned the unselected areas as training data to appropriate classes.

Table 4. The results of the confusion matrix for the classifications performed using ASTER images.

Classification	Overall Acc	Kappa coefficient
A-1	83.50%	0.8075
A-2	64.17%	0.6019

10. Validation

Validation remote sensing refers to evaluating and analyzing the accuracy of data and information. The main objective of validation is to examine the accuracy and reliability of data and results obtained from remote sensing processes. This evaluation includes comparing and aligning the data with reference data, examining the technical and scientific accuracy of the remote sensing process, and verifying the accuracy and efficiency of the methods and algorithms used [69].

In general, validation in remote sensing is essential to ensure the accuracy and correctness of the data, improve the performance and accuracy of the results, evaluate methods and algorithms, and optimize the utilization of classification results. In this case, using the 1:100,000 geological map of the Sar-e-châh-e-shur region and image analysis methods, the available geological information is identified, land surfaces are classified, and more detailed and specific geological information is detected. This approach allows us to examine and analyze the level of agreement between numerous maps and the geological map of the region.

Finally, using this method, we can comprehend and evaluate the validity and accuracy of the performed classifications depicted on the maps. Based on the provided explanations, in Figure 4, the combination of maps associated with each of the introduced classifications is demonstrated alongside the geological map of the Sar-e-châh-e-shur region. This allows us to indicate the level of conformity achieved between the output results of image classification for the study area compared to the geological map of the region.

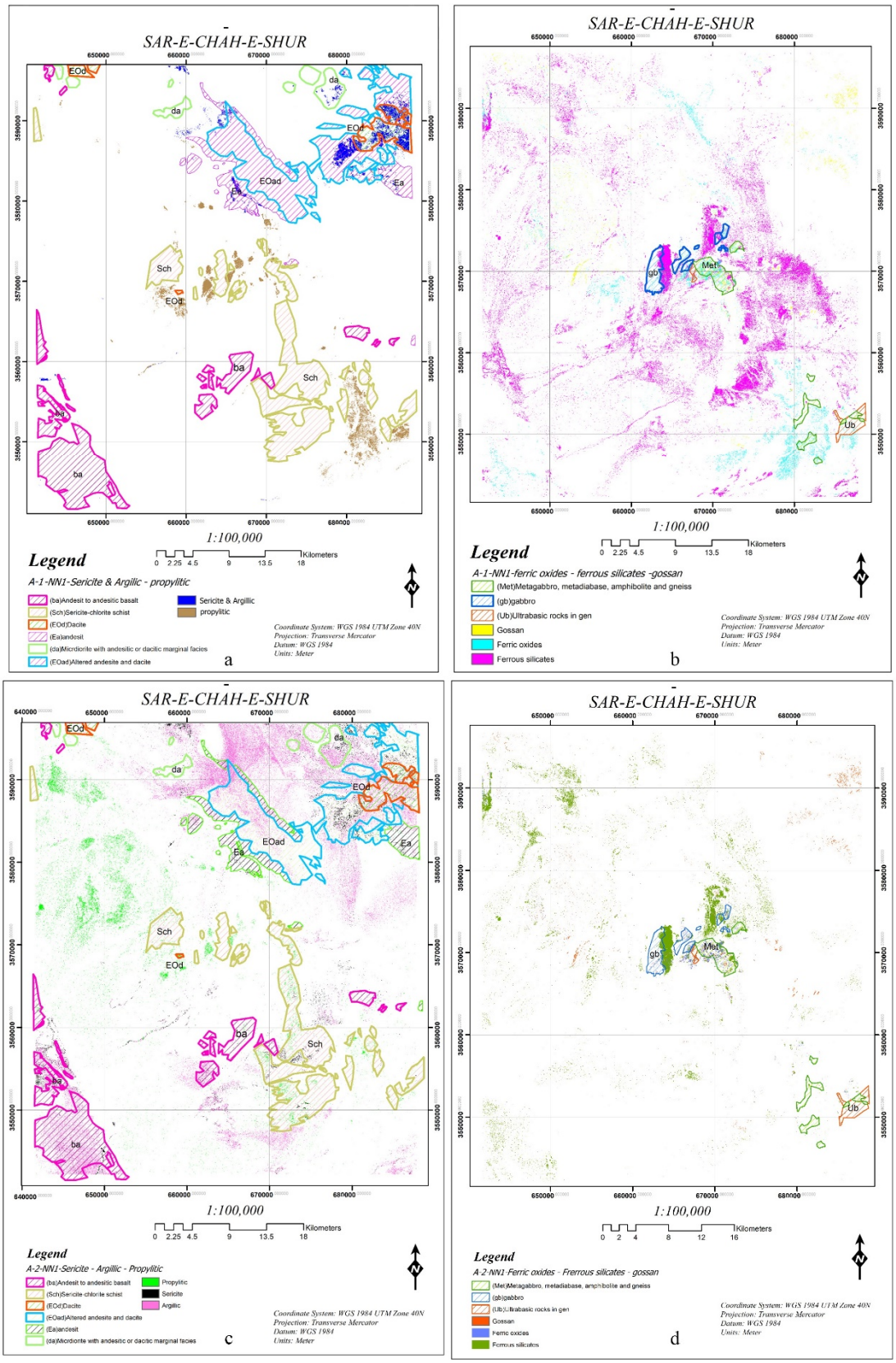

Figure 5. The integration of the abundance map (a) A-1-NN1-s-a-p (Sericite, Argillic, and Propylitic) (b) A-1-NN1-Iron (ferric oxides, ferrous silicates, and Gossan) (c) A-2-NN1-s-a-p. (Sericite, Argillic, and Propylitic) (d) A-2-NN1-Iron (ferric oxides, ferrous silicates, and Gossan) with the relevant geological map.

In this scenario, considering Table 4 and examining the validation maps, we performed the conclusion using the Normal Score (NS) equation on the outputs of the neural network algorithm. We have established this equation to transform qualitative measures into quantitative ones to gain a better understanding of the validation level and ultimately facilitate the final decision-making process. In this equation, C represents the coverage level of the desired geological units, and E indicates the accuracy level of estimation, which is calculated using the recommended values in Table 5. Furthermore, to better understand the Normal Score, we have created the formula NSP (Normal Score percentage), and its results are presented in Table 6.

$$NS = \sum_{1}^{n} \frac{C_n \times E_n}{N}$$

$$NSP = 25 \times NS$$

$$0 \leq NS \leq 4$$

$$0 \leq NSP \leq 100$$

NS = Normal Score

NSP = Normal Score Percentage

C = Compliance

E = Estimate

n = The class number

N = The number of maps used for category classification validation

Table 5. Conversion of qualitative to quantitative criteria

Compliance	Estimate
Non-compliance: 0	Overestimate: 0
Partial compliance: 1	Partial estimate: 0.25
Semi-compliance: 2	Semi-estimate: 0.5
Almost compliance: 3	Almost estimate: 0.75
Perfect compliance: 4	Perfect estimate: 1

Table 6. The validation results of class scores are based on the normalized scores.

Alteration	Normal score percentage	Normal score	Estimated rate	Compliance with geological units	Classes name
Porphyry copper, iron	٪41	1.625	0.75	3	A-1-NN1-Iron
			0.5	2	A-1-NN1-s-a-p
Advanced argillic, **iron**	٪56	2.25	0.75	4	A-2-NN1s-a-p
			0.5	3	A-2-NN1-Iron

According to the obtained results in Table 6, the A-1 category, which represents the maps of porphyry copper alteration, has achieved a score of 1.625 out of 4, indicating a 41% level of conformity with the geological map of the region. Additionally, the A-2 category, representing the maps of advanced argillic alteration, has obtained the highest score (2.25 out of 4), indicating a 56% level of conformity with the geological map of the region. This is considered an acceptable outcome.

11. Conclusions

ASTER data is a useful tool for examining and identifying hydrothermal alteration zones related to porphyry copper and iron-rich zones. Hydrothermal alteration zones related to porphyry copper such as phyllic, argillic, potassic, and propylitic zones, can be distinguished from each other. The distinction between phyllic, argillic, and propylitic zones can indicate the highest desired mineralization potential, which is usually associated with altered phyllic zones. ASTER data can be processed and analyzed in the best possible way to obtain information about the spatial distribution of hydrothermal alteration zones related to porphyry copper worldwide, including undiscovered areas.

The reason for studying the sar-e-châh-e-shur region is the special geological conditions including its proximity to the Lut Block and the occurrence of the collapse phenomenon. The mineralizations associated with porphyry copper are highly dependent on these areas, and the results of the conducted classifications provide a clear reason for this claim. In this research work, after performing the necessary preprocessing, two categories, A-1 and A-2, were created using the introduced band ratios. Then using a neural network algorithm, the entire region was classified. In this case, despite the lower accuracy compared to the A-1 category, the good conformity of the classification results of the A-2 category with advanced argillic alteration (Figure 3-i) to the existing reality and the geological map (Figure 1) is observed. Furthermore, susceptible zones for copper mineralization in the central and northeastern sectors of the specified area were delineated. Moreover, there are promising zones

within the central region of the locality that merit additional scrutiny for iron exploration.

References

[1]. Tagwai, M. G., Jimoh, O. A., Shehu, S. A., & Zabidi, H. (2023). Application of GIS and remote sensing in mineral exploration: current and future perspectives. *World Journal of Engineering*.

[2]. Schowengerdt, R. A. (2007). *Remote sens: models and methods for image processing*. Elsevier/Academic Press, Oxford.

[3]. Guo, H., Huang, Q., Li, X., Sun, Z., & Zhang, Y. (2013). Spatiotemporal analysis of urban environment based on the vegetation–impervious surface–soil model. *Journal of Applied Remote Sensing*, *8*(1), 84597.

[4]. Schott, J. R. (2007). *Remote sensing: the image chain approach*. Oxford University Press on Demand.

[5]. Ferriere, G., & Wadge, G. (1996). The application of imaging spectrometry data to mapping alteration zones associated with gold mineralization in southern Spain. *International Journal of Remote Sensing*, *17*(2), 331–350.

[6]. Ferrier, G., White, K., Griffiths, G., Bryant, R., & Stefouli, M. (2002). The mapping of hydrothermal alteration zones on the island of Lesvos, Greece using an integrated remote sensing dataset. *International Journal of Remote Sensing*, *23*(2), 341–356.

[7]. Hunt, G. R., & Ashley, R. P. (1979). Spectra of altered rocks in the visible and near infrared. *Economic Geology*, *74*(7), 1613–1629.

[8]. Abrams, M. J., & Brown, D. (1984). Silver Bell, Arizona, porphyry copper test site report: Tulsa, Oklahoma. *The American Association of Petroleum Geologists, the Joint NASA–Geosat Test Case Project, Final Report*, 4–73.

[9]. Abrams, M. J., Brown, D., Lepley, L., & Sadowski, R. (1983). Remote sensing for porphyry copper deposits in southern Arizona. *Economic Geology*, *78*(4), 591–604.

[10]. Spatz, D. M., Wilson, R. T., Pierce, F. W., & Bolm, J. G. (1995). Remote sensing characteristics of porphyry copper systems, western America Cordillera. *Arizona Geological Society Digest*, *20*, 94–108.

[11]. Lowell, J. D., & Guilbert, J. M. (1970). Lateral and vertical alteration-mineralization zoning in porphyry ore deposits. *Economic Geology*, *65*(4), 373–408.

[12]. Abdelsalam, M. G., Stern, R. J., & Berhane, W. G. (2000). Mapping gossans in arid regions with Landsat TM and SIR-C images: the Beddaho Alteration Zone in northern Eritrea. *Journal of African Earth Sciences*, *30*(4), 903–916.

[13]. Sabins, F. F. (1999). Remote sensing for mineral exploration. *Ore Geology Reviews*, *14*(3–4), 157–183.

[14]. Hunt, G. R. (1977). Spectral Signatures of Particulate Minerals in The Visible and Near Infrared. *GEOPHYSICS*, *42*(3), 501–513.

[15]. Clark, R. N., King, T. V. V, Klejwa, M., Swayze, G. A., & Vergo, N. (1990). High spectral resolution reflectance spectroscopy of minerals. *Journal of Geophysical Research*, *95*(B8), 12653.

[16]. Crowley, J. K. (1988). Near-Infrared Reflectance Spectra of Mixtures of Kaolin-Group Minerals: Use in Clay Mineral Studies. *Clays and Clay Minerals*, *36*(4), 310–316.

[17]. Huntington, J. F. (2007). The Role of Remote Sensing in Finding Hydrothermal Mineral Deposits on Earth. In *Ciba Foundation Symposium 202-Evolution of Hydrothermal Ecosystems on Earth (and Mars?) Evolution of Hydrothermal Ecosystems on Earth (and Mars?): Ciba Foundation Symposium 202* (pp. 214–235). Wiley Online Library.

[18]. Bedini, E., van der Meer, F., & van Ruitenbeek, F. (2009). Use of HyMap imaging spectrometer data to map mineralogy in the Rodalquilar caldera, southeast Spain. *International Journal of Remote Sensing*, *30*(2), 327–348.

[19]. Di Tommaso, I., & Rubinstein, N. (2007). Hydrothermal alteration mapping using ASTER data in the Infiernillo porphyry deposit, Argentina. *Ore Geology Reviews*, *32*(1–2), 275–290.

[20]. Gabr, S., Ghulam, A., & Kusky, T. (2010). Detecting areas of high-potential gold mineralization using ASTER data. *Ore Geology Reviews*, *38*(1–2), 59–69.

[21]. Kruse, F. A., Boardman, J. W., & Huntington, J. F. (2003). Comparison of airborne hyperspectral data and eo-1 hyperion for mineral mapping. *IEEE Transactions on Geoscience and Remote Sensing*, *41*(6), 1388–1400.

[22]. Rowan, L. C., Schmidt, R. G., & Mars, J. C. (2006). Distribution of hydrothermally altered rocks in the Reko Diq, Pakistan mineralized area based on spectral analysis of ASTER data. *Remote Sensing of Environment*, *104*(1), 74–87.

[23]. Moore, F., Rastmanesh, F., Asadi, H., & Modabberi, S. (2008). Mapping mineralogical alteration using principal-component analysis and matched filter processing in the Takab area, north-west Iran, from ASTER data. *International Journal of Remote Sensing*, *29*(10), 2851–2867.

[24]. Perry, S. L. (2004). Spaceborne and airborne remote sensing systems for mineral exploration-case histories using infrared spectroscopy. *Infrared Spectroscopy in Geochemistry, Exploration Geochemistry, and Remote Sensing*, *33*, 227–240.

[25]. Pour, B. A., Hashim, M., & Marghany, M. (2011). Using spectral mapping techniques on short wave infrared bands of ASTER remote sensing data for

alteration mineral mapping in SE Iran. *Int. J. Phys. Sci*, *6*(4), 917–929.

[26]. Tangestani, M. H., & Moore, F. (2002). Porphyry copper alteration mapping at the Meiduk area, Iran. *International Journal of Remote Sensing*, *23*(22), 4815–4825.

[27]. Tangestani, M. H., Mazhari, N., Agar, B., & Moore, F. (2008). Evaluating Advanced Spaceborne Thermal Emission and Reflection Radiometer (ASTER) data for alteration zone enhancement in a semi-arid area, northern Shahr-e-Babak, SE Iran. *International Journal of Remote Sensing*, *29*(10), 2833–2850.

[28]. Zhang, X., Pazner, M., & Duke, N. (2007). Lithologic and mineral information extraction for gold exploration using ASTER data in the south Chocolate Mountains (California). *ISPRS Journal of Photogrammetry and Remote Sensing*, *62*(4), 271–282.

[29]. Abrams, M., & Yamaguchi, Y. (2019). Twenty Years of ASTER Contributions to Lithologic Mapping and Mineral Exploration. *Remote Sensing*, *11*(11), 1394.

[30]. Richards, J. A. (2013). Feature Reduction. In *Remote Sensing Digital Image Analysis* (pp. 343–380). Springer Berlin Heidelberg.

[31]. Karimpour, M. H., Mazhari, N., & Shafaroudi, A. M. (2014). Discrimination of Different Erosion Levels of Porphyry Cu Deposits using ASTER Image Processing in Eastern Iran: a Case Study in the Maherabad, Shadan, and Chah Shaljami Areas. *Acta Geologica Sinica - English Edition*, *88*(4), 1195–1213.

[32]. Mohebi, A., Mirnejad, H., Lentz, D., Behzadi, M., Dolati, A., Kani, A., & Taghizadeh, H. (2015). Controls on porphyry Cu mineralization around Hanza Mountain, south-east of Iran: An analysis of structural evolution from remote sensing, geophysical, geochemical and geological data. *Ore Geology Reviews*, *69*, 187–198.

[33]. Sojdehee, M., Rasa, I., Nezafati, N., & Abedini, M. V. (2016). Application of spectral analysis to discriminate hydrothermal alteration zones at Daralu copper deposit, SE Iran. *Arabian Journal of Geosciences*, *9*(1), 41.

[34]. Farahbakhsh, E., Shirmard, H., Bahroudi, A., & Eslamkish, T. (2016). Fusing ASTER and QuickBird-2 Satellite Data for Detailed Investigation of Porphyry Copper Deposits using PCA; Case Study of Naysian Deposit, Iran. *Journal of the Indian Society of Remote Sensing*, *44*(4), 525–537.

[35]. Yousefi, S. J., Ranjbar, H., Alirezaei, S., & Dargahi, S. (2018). Discrimination of Sericite Phyllic and Quartz-Rich Phyllic Alterations by Using a Combination of ASTER TIR and SWIR Data to Explore Porphyry Cu Deposits Hosted by Granitoids, Kerman Copper Belt, Iran. *Journal of the Indian Society of Remote Sensing*, *46*(5), 717–727. https://doi.org/10.1007/s12524-017-0745-z

[36]. Yousefi, S. J., Ranjbar, H., Alirezaei, S., Dargahi, S., & Lentz, D. R. (2018). Comparison of hydrothermal alteration patterns associated with porphyry Cu deposits hosted by granitoids and intermediate-mafic volcanic rocks, Kerman Magmatic Arc, Iran: Application of geological, mineralogical and remote sensing data. *Journal of African Earth Sciences*, *142*, 112–123.

[37]. Pour, A. B., & Hashim, M. (2012). Identifying areas of high economic-potential copper mineralization using ASTER data in the Urumieh–Dokhtar Volcanic Belt, Iran. *Advances in Space Research*, *49*(4), 753–769.

[38]. Honarpazhouh, J., Hassanipak, A. A., & Shabani, K. S. (2013). Integration of stream sediment geochemical and ASTER data for porphyry copper deposit exploration in Khatun Abad, North West of Iran. *Archives of Mining Sciences*, *58*(1).

[39]. Pazand, K., Sarvestani, J. F., & Ravasan, M. R. S. (2013). Hydrothermal Alteration Mapping Using ASTER Data for Reconnaissance Porphyry Copper Mineralization in the Ahar Area, NW Iran. *Journal of the Indian Society of Remote Sensing*, *41*(2), 379–389.

[40]. Alimohammadi, M., Alirezaei, S., & Kontak, D. J. (2015). Application of ASTER data for exploration of porphyry copper deposits: A case study of Daraloo–Sarmeshk area, southern part of the Kerman copper belt, Iran. *Ore Geology Reviews*, *70*, 290–304.

[41]. Yazdi, Z., Jafari Rad, A. R., & Ajayebi, K. S. (2015). Analysis and modeling of geospatial datasets for porphyry copper prospectivity mapping in Chahargonbad area, Central Iran. *Arabian Journal of Geosciences*, *8*(10), 8237–8248.

[42]. Mars, J. (2006). Regional mapping of phyllic- and argillic-altered rocks in the Zagros magmatic arc, Iran, using Advanced Spaceborne Thermal Emission and Reflection Radiometer (ASTER) data and logical operator algorithms. *Geosphere*, *2*(3), 161.

[43]. Carrino, T. A., Crosta, A. P., Toledo, C. L. B., Silva, A. M., & Silva, J. L. (2015). Geology and Hydrothermal Alteration of the Chapi Chiara Prospect and Nearby Targets, Southern Peru, Using ASTER Data and Reflectance Spectroscopy. *Economic Geology*, *110*(1), 73–90.

[44]. Rajendran, S., & Nasir, S. (2017). Characterization of ASTER spectral bands for mapping of alteration zones of volcanogenic massive sulphide deposits. *Ore Geology Reviews*, *88*, 317–335. https://doi.org/10.1016/j.oregeorev.2017.04.016

[45]. Zhang, N., & Zhou, K. (2017). Identification of hydrothermal alteration zones of the Baogutu porphyry copper deposits in northwest China using ASTER data. *Journal of Applied Remote Sensing*, *11*(1), 15016.

[46]. Dai, J., Qu, X., & Song, Y. (2018). Porphyry Copper Deposit Prognosis in the Middle Region of the Bangonghu-Nujiang Metallogenic Belt, Tibet, Using

ASTER Remote Sensing Data. *Resource Geology*, *68*(1).

[47]. Kurzawa, T., Bröcker, M., Rad, G. F., Berndt, J., & Lisker, F. (2017). Cretaceous high-pressure metamorphism and low pressure overprint in the Sistan Suture Zone, eastern Iran: Additional temperature estimates for eclogites, geological significance of U-Pb zircon ages and Rb-Sr constraints on the timing of exhumation. *Journal of Asian Earth Sciences*, *147*, 332–344.

[48]. Karimpour, M. H., Zarrinkoub, M. H., & Sadeghi, M. (1996). *Project of producing mineral potential map in eastern Iran». Department of Geology, University of Birjand*.

[49]. Vassigh, H., & Soheili, M. (1975). Geological Map of Sar-e-chah-e-shur (1: 100000). *Geological Survey of Iran (GSI)*.

[50]. Green, A. A., & Craig, M. D. (1985). Analysis of aircraft spectrometer data with logarithmic residuals. *JPL Proc. of the Airborne Imaging Spectrometer Data Anal. Workshop*.

[51]. Ghassemian, H. (2016). A review of remote sensing image fusion methods. *Information Fusion*, *32*, 75–89.

[52]. Ibrahim, W. S., Watanabe, K., & Yonezu, K. (2016). Structural and litho-tectonic controls on Neoproterozoic base metal sulfide and gold mineralization in North Hamisana shear zone, South Eastern Desert, Egypt: The integrated field, structural, Landsat 7 ETM + and ASTER data approach. *Ore Geology Reviews*, *79*, 62–77.

[53]. Salisbury, J. W., Hunt, G. R., & Lenhoff, C. J. (1975). Visible and near-infrared spectra: X. Stony meteorites. *Modern Geology*, *5*, 115–126.

[54]. Kalinowski, A., & Oliver, S. (2004). *ASTER Mineral Index Processing Manual, Remote Sensing Applications Geoscience Australia October 2004, pages 22,23.* 22–23.

[55]. Soleimani, S. (1998). *Investigating the types of gosans and their use in the exploration of mineral reserves in Kerman province (In Persian)* (p. 1).

[56]. Volesky, J. C., Stern, R. J., & Johnson, P. R. (2003). Geological control of massive sulfide mineralization in the Neoproterozoic Wadi Bidah shear zone, southwestern Saudi Arabia, inferences from orbital remote sensing and field studies. *Precambrian Research*, *123*(2–4), 235–247.

[57]. Hosseini, M. (2021). *Discrimination of Hydrothermal Alterations Associated with Copper Mineralization using ASTER Image Processing Sheet in Sar-e-Chah-e-Shur, Eastern Iran* (Vol. 18, Issue 1).

[58]. Oliver, S., & Kalinowski, A. (2004). *ASTER Mineral Index Processing Manual*. Remote Sensing Applications Geoscience Australia.

[59]. Cudahy, T. J., Okada, K., Cornelius, A., & Hewson, R. D. (2002). Regional to prospect scale exploration for porphyry-skarn-epithermal mineralisation at Yerington, Nevada, using ASTER and airborne Hyperspectral data. *CSIRO Exploration and Mining Report*.

[60]. Richards, J. A., & Jia, X. (1999). *Remote Sensing Digital Image Analysis*. Springer Berlin Heidelberg.

[61]. Goodfellow, I., Bengio, Y., & Courville, A. (2016). *Deep learning*. MIT press.

[62]. Wang, R., Bu, F., Jin, H., & Li, L. (2007). A Feature-Level Image Fusion Algorithm based on Neural Networks. *2007 1st International Conference on Bioinformatics and Biomedical Engineering*, 821–824.

[63]. Haykin, S. (1998). *Neural networks: a comprehensive foundation*. Prentice Hall PTR.

[64]. LeCun, Y., Bengio, Y., & Hinton, G. (2015). Deep learning. *Nature*, *521*(7553), 436–444.

[65]. Zhang, X., & LeCun, Y. (2015). Text understanding from scratch. *ArXiv Preprint ArXiv:1502.01710*.

[66]. Schmidhuber, J. (2015). Deep learning in neural networks: An overview. *Neural Networks*, *61*, 85–117.

[67]. Bishop, C. M., & Nasrabadi, N. M. (2006). *Pattern recognition and machine learning* (Vol. 4, Issue 4). Springer.

[68]. Muavhi, N. (2022). Evaluation of effectiveness of supervised classification algorithms in land cover classification using ASTER images-A case study from the Mankweng (Turfloop) Area and its environs, Limpopo Province, South Africa. *South African Journal of Geomatics*, *9*(1), 61–74.

[69]. Jensen, J. R. (1986). *Introductory Digital Image Processing: A Remote Sensing Perspective*.

طبقه‌بندی داده‌های استر با استفاده از شبکه عصبی برای نقشه‌برداری آلتراسیون های مرتبط با کانی‌سازی مس و آهن در بیرجند

جبار حبش[1]، مجید محمدی اسکویی[2]*، هادی جمشید مقدم[3]

1- کارشناسی ارشد. دانشکده مهندسی معدن، دانشگاه صنعتی سهند، تبریز، ایران

2- استاد دانشکده مهندسی معدن، دانشگاه صنعتی سهند، تبریز، ایران.

3-دکترای رشته مهندسی اکتشاف معدن، رئیس بخش تحقیق و توسعه گروه سرمایه گذاری فولادگستر کوثر.

ارسال 2023/09/20، پذیرش 2023/11/12

* نویسنده مسئول مکاتبات:mohammady@sut.ac.ir

چکیده:

منطقه مورد مطالعه واقع در شرق ایران، به دلیل رژیم تکتونیکی فعال، پتانسیل بسیار بالایی برای انواع کانی‌زایی، به ویژه مس، دارد. با وجود پوشش گیاهی ناچیز، داده‌های سنجش از دور می‌توانند مناطق دگرسان شده را به خوبی تشخیص دهند. در این مطالعه، از داده‌های چندطیفی استر برای شناسایی دگرسانی‌های مرتبط با آلتراسیونهای آرژیلیک، سریسیت، پروپیلیتیک و اکسیدهای آهن مرتبط با کانی سازی مس استفاده شد. برای این منظور، دو دسته خوشه کلاسی مرتبط با دگرسانی‌ها (مس پورفیری-آهن و آرژیلیک پیشرفته-آهن) را برای انجام طبقه‌بندی در منطقه به مساحت ۲۶۱۷ کیلومتر مربع با استفاده از الگوریتم شبکه عصبی در نظر گرفته شد. برای ارزیابی صحت طبقه‌بندی نیز از دو مؤلفه صحت کلی و ضریب کاپا، که با استفاده از ماتریس ابهام محاسبه می‌شوند، استفاده گردید. در این حالت، خوشه‌های کلاسی آرژیلیک پیشرفته و مس پورفیری به ترتیب صحت کلی ٪۶۴.۱۷ و ٪۸۳.۵ و ضریب کاپا ۰.۶۰۲ و ۰.۸۰۷ را کسب کردند. در نهایت، برای اعتبارسنجی طبقه‌بندی‌ها از معیارهای کمی در معادله امتیاز نرمال شده استفاده شد. در این حالت، خوشه کلاسی آرژیلیک پیشرفته به بالاترین امتیاز نرمال (۲.۲۵ از ۴) دست یافت که نشان‌دهنده انطباق ۵۶ درصدی با واقعیت‌های زمین‌شناسی منطقه داشت. این امر منجر به شناسایی مناطق مطلوب در بخش‌های مرکزی و شمال شرقی منطقه مورد مطالعه شد.

کلمات کلیدی: سنجش از دور، استر، شبکه عصبی، مس پورفیری، آرژیلیک پیشرفته، طبقه بندی، امتیاز نرمال شده.